

618416
P28

1N-02
157153

Navier-Stokes Simulation of Transonic Wing Flow Fields Using a Zonal Grid Approach

Neal M. Chaderjian

(NASA-TM-100039) NAVIER-STOKES SIMULATION
OF TRANSONIC WING FLOW FIELDS USING A ZONAL
GRID APPROACH (NASA) 26 P CSCL 01A

N89-10022

G3/02 Unclass
0157153

January 1988



National Aeronautics and
Space Administration

Navier-Stokes Simulation of Transonic Wing Flow Fields Using a Zonal Grid Approach

Neal M. Chaderjian, Ames Research Center, Moffett Field, California

January 1988



National Aeronautics and
Space Administration

Ames Research Center
Moffett Field, California 94035

NAVIER-STOKES SIMULATION OF TRANSONIC WING FLOW FIELDS USING A ZONAL GRID APPROACH

SUMMARY

The transonic Navier-Stokes code was used to simulate flow fields about isolated wings for workshop wind-tunnel and free-air cases using the thin-layer Reynolds-averaged Navier-Stokes equations. An implicit finite-difference scheme based on a diagonal version of the Beam-Warming algorithm was used to integrate the governing equations. A zonal grid approach was used to allow efficient grid refinement near the wing surface. The flow field was sensitive to the turbulent transition model, and flow unsteadiness was observed for a wind-tunnel case but not for the corresponding free-air case. The specification of experimental pressure at the wind-tunnel exit plane is the primary reason for the difference of these two numerical solutions.

INTRODUCTION

In the past, aircraft companies have relied heavily upon simplified theory, wind-tunnel experiments, and flight-test data to facilitate the aircraft design process. However, computational fluid dynamics (CFD) has emerged as a new tool that is taking on an increasingly important role in the design process. This is primarily due to recent improvements in super computer speed and memory, as well as to similar improvements in efficient numerical algorithms [1-2]. Consequently, it is now possible to simulate complex three-dimensional (3-D) aerodynamic flows that are of current and practical interest. For example, CFD has been used to study the formation of wing-tip vortices, vortex bursting, flow separation, turbulence modeling, and flow fields about aircraft [3-6].

It is the purpose of this workshop to shed some light on the current state-of-the-art capabilities of CFD in simulating aerodynamic flow fields. Several scientists working on numerical methods for the compressible Navier-Stokes equations have been invited to simulate the viscous flow field about a finite wing in a wind tunnel. The experiment was designed to be a well-defined boundary value problem suitable for CFD simulations. A computer code was supplied to workshop participants to define the shape of the wing, and a description of the wind-tunnel test section with closed walls was also provided. The experimental flow field was completely defined at the inflow boundary, including the boundary layer profiles at the walls, and also provided was the exit plane static pressure. Finally, a transition line where the flow can be considered fully turbulent was given from experimental data. The workshop organizers will compare the experimental data with the numerical solutions supplied by the workshop participants.

The transonic Navier-Stokes code (TNS) at NASA Ames Research Center was used to compute the workshop cases on a Cray 2 super computer. This finite-difference code applies the thin-layer Reynolds-averaged Navier-Stokes equations to isolated wing geometries (free-air cases) or wings mounted in a wind tunnel [7]. A zonal grid approach is adopted to

facilitate the treatment of complex geometries. The TNS code uses the Baldwin-Lomax algebraic turbulence model primarily because it is efficient for practical 3-D computations [8].

The solution of the workshop cases consisted of four steps. First, the grid on the wing surface was generated using the program supplied by Sobieczky [9]. All cases in this paper used 55 grid points on the upper wing surface in the streamwise direction, 55 grid points on the lower surface, and 35 grid points in the spanwise direction. Second, a coarse global grid (H-H type) was generated using an elliptic Poisson equation method of Sorenson [10]. Considerable effort was made to control grid skewness, smoothness, and spacing near the wing surface and computational boundaries. Three dimensional grid generation is still relatively new, and this particular wing geometry proved to be rather tedious. Third, a grid zoning program was used to subdivide the coarse global grid into four zones. Each zone was refined as appropriate to capture the proper flow physics. Finally, the TNS flow solver code was used to simulate the flow field for the different workshop cases.

GOVERNING EQUATIONS

The thin-layer Reynolds-averaged Navier-Stokes equations are written in generalized curvilinear coordinates and in strong conservation-law form as

$$\partial_\tau \hat{Q} + \partial_\xi \hat{E} + \partial_\eta \hat{F} + \partial_\zeta \hat{G} = Re^{-1} \partial_\zeta \hat{S}, \quad (1)$$

where

$$\begin{aligned} \hat{Q} &= J^{-1} \begin{bmatrix} \rho \\ \rho u \\ \rho v \\ \rho w \\ e \end{bmatrix}, \quad \hat{E} = J^{-1} \begin{bmatrix} \rho U \\ \rho u U + \xi_x p \\ \rho v U + \xi_y p \\ \rho w U + \xi_z p \\ U(e + p) - \xi_t p \end{bmatrix}, \\ \hat{F} &= J^{-1} \begin{bmatrix} \rho V \\ \rho u V + \eta_x p \\ \rho v V + \eta_y p \\ \rho w V + \eta_z p \\ V(e + p) - \eta_t p \end{bmatrix}, \quad \hat{G} = J^{-1} \begin{bmatrix} \rho W \\ \rho u W + \zeta_x p \\ \rho v W + \zeta_y p \\ \rho w W + \zeta_z p \\ W(e + p) - \zeta_t p \end{bmatrix}, \\ \hat{S} &= J^{-1} \begin{bmatrix} 0 \\ \mu m_1 u_\zeta + (\mu/3) m_2 \zeta_x \\ \mu m_1 v_\zeta + (\mu/3) m_2 \zeta_y \\ \mu m_1 w_\zeta + (\mu/3) m_2 \zeta_z \\ \mu m_1 m_3 + (\mu/3) m_2 (\zeta_x u + \zeta_y v + \zeta_z w) \end{bmatrix}, \end{aligned}$$

with $m_1 = \zeta_x^2 + \zeta_y^2 + \zeta_z^2$, $m_2 = \zeta_x u_\zeta + \zeta_y v_\zeta + \zeta_z w_\zeta$, and $m_3 = .5(u^2 + v^2 + w^2)_\zeta + Pr^{-1}(\gamma - 1)^{-1}(a^2)_\zeta$. In the above expression the scaled contravariant velocity components are defined by

$$U = \xi_t + \xi_x u + \xi_y v + \xi_z w, \quad (2a)$$

$$V = \eta_t + \eta_x u + \eta_y v + \eta_z w, \quad (2b)$$

$$W = \zeta_t + \zeta_x u + \zeta_y v + \zeta_z w, \quad (2c)$$

and the pressure is related to the other flow variables by the perfect gas law

$$p = (\gamma - 1) \left[e - \frac{1}{2} \rho (u^2 + v^2 + w^2) \right]. \quad (3)$$

The transformation metrics are defined as

$$\begin{aligned} \xi_x &= J(y_\eta z_\zeta - z_\eta y_\zeta), \quad \eta_x = J(z_\xi y_\zeta - y_\xi z_\zeta), \\ \xi_y &= J(z_\eta x_\zeta - x_\eta z_\zeta), \quad \eta_y = J(x_\xi z_\zeta - z_\xi x_\zeta), \\ \xi_z &= J(x_\eta y_\zeta - y_\eta x_\zeta), \quad \eta_z = J(y_\xi x_\zeta - x_\xi y_\zeta), \\ \zeta_x &= J(y_\xi z_\eta - z_\xi y_\eta), \quad \xi_t = -x_\tau \xi_x - y_\tau \xi_y - z_\tau \xi_z, \\ \zeta_y &= J(z_\xi x_\eta - x_\xi z_\eta), \quad \eta_t = -x_\tau \eta_x - y_\tau \eta_y - z_\tau \eta_z, \\ \zeta_z &= J(x_\xi y_\eta - y_\xi x_\eta), \quad \zeta_t = -x_\tau \zeta_x - y_\tau \zeta_y - z_\tau \zeta_z, \end{aligned} \quad (4)$$

and the Jacobian by

$$J^{-1} = x_\xi(y_\eta z_\zeta - z_\eta y_\zeta) + x_\eta(z_\xi y_\zeta - y_\xi z_\zeta) + x_\zeta(x_\xi z_\eta - z_\xi y_\eta). \quad (5)$$

A choice of two implicit approximate-factorization algorithms are available in TNS to integrate Eq. (1). The first option is the Beam-Warming algorithm [11] given by

$$\begin{aligned} (I + h\delta_\xi \hat{A}^n - hD_i|_\xi)(I + h\delta_\eta \hat{B}^n - hD_i|_\eta) \\ (I + h\delta_\zeta \hat{C}^n - hRe^{-1}\bar{\delta}_\zeta J^{-1}\hat{M}^n J - hD_i|_\zeta)\Delta\hat{Q}^n = \hat{R}^n, \end{aligned} \quad (6)$$

where

$$\hat{R}^n = -h(\delta_\xi \hat{E}^n + \delta_\eta \hat{F}^n + \delta_\zeta \hat{G}^n - Re^{-1}\bar{\delta}_\zeta \hat{S}^n + D_e \hat{Q}^n).$$

In the above expression \hat{A} , \hat{B} , \hat{C} , and \hat{M} , are the Jacobian matrices of \hat{E} , \hat{F} , \hat{G} , and \hat{S} , respectively. The numerical metrics are evaluated so that uniform flow is an exact solution of the finite-difference equations as described by Chaderjian [12]. The above method is second-order accurate in time (trapezoidal rule) when $h = \frac{1}{2}\Delta t$ in the implicit side, and first-order accurate (Euler implicit) when $h = \Delta t$. The spatial operators use central differencing throughout, so fourth-order explicit (D_e) and second-order implicit (D_i) numerical dissipation terms are added in order to damp any high-frequency errors. This method requires the solution of a block tridiagonal system of equations which is computationally costly. For more details of this algorithm, see Pulliam and Steger [13]. The second option is a diagonal form of the Beam-Warming algorithm developed by Pulliam and Chaussee [14]. It has the form

$$T_\xi(I + h\delta_\xi \Lambda_\xi^n + hD_i|_\xi)\hat{N}(I + h\delta_\eta \Lambda_\eta^n + hD_i|_\eta)\hat{P}(I + h\delta_\zeta \Lambda_\zeta^n + hD_i|_\zeta)T_\xi^{-1}\Delta\hat{Q}^n = \hat{R}^n, \quad (7)$$

where Λ_ξ is a diagonal matrix consisting of the eigenvalues of \hat{A} , and so on. The diagonal algorithm, Eq. (7), uses fourth-order explicit and implicit numerical dissipation, is first-order accurate in time, and only requires the solution of scalar pentadiagonal equations. The right hand side of Eq. (7) is identical to the right hand side of the Beam-Warming algorithm, Eq. (6), with the exception of the dissipation terms. Both the explicit and implicit dissipation terms are scaled by the sum of the spectral radii of the Jacobian matrices \hat{A} , \hat{B} , and \hat{C} . The diagonal algorithm was used for the computations presented in this paper.

Convergence to a steady-state solution can be accelerated by using local time stepping. Two methods are used in the TNS code: one is based on the local Courant number, and the second is based on the local grid Jacobian given by Srinivasan et al [15]

$$h = \frac{\Delta t_0}{1 + \sqrt{J}}, \quad (8)$$

where Δt_0 is a user specified constant. Flores [16], using the diagonal algorithm with Eq. (8), reported convergence rates 40 times those obtained using the Beam-Warming algorithm with constant time step. Local time stepping with Eq. (8) was used to obtain the results in this paper.

ZONAL APPROACH

A zonal grid approach has been adopted in the TNS code in order to treat complex geometries, e.g., the F-16 fighter aircraft [6]. There are several advantages in using a zonal approach. First, it can be difficult, if not impossible, to generate a single grid about a complex geometry with adequate grid clustering to resolve the flow physics. One could divide a complex configuration into simply shaped zones so that each zone could be refined in a straight forward manner. Moreover, different zonal topologies can be used to better represent the surface geometry. Second, grid clustering near a body surface with a single grid wastes grid points in the far field where they are not needed. Third, a zonal approach can help combat main memory restrictions on machines such as the Cray XM-P that have a solid state device (SSD), an efficient mass storage device. Only one zonal grid and its solution variables need reside in main memory while the other zones are stored on the SSD. The data can be transferred between main memory and the SSD as needed. The present computations were performed at NASA Ames Research Center on the Numerical Aerodynamic Simulation Facility's (NAS) Cray 2 which has 256 million words of main memory. The TNS code and all four zones required 24 million words and were kept in main memory.

Zonal Grid Topology

The computational regime about the DFVLR-F5 wing is subdivided into four zones, or grids, with a plane of symmetry at the wing root (splitter plate for wind-tunnel cases). A cross-sectional view of the four zones is shown in Fig. (1) as well as a planform view of the upper wing surface. The coarse outer grid, zone 1, is supplied from the grid-generation program and has a cut-out region that is occupied by three finer grids supplied from the

grid-zoning program. Throughout the rest of this paper terms such as zone, grid, and block are used interchangeably.

The grid-zoning program takes block 1 and fills the empty region with block 2, [see Fig. (1b)]. Like block 1, block 2 also has a cut-out region about the wing. The viscous terms are turned off in blocks 1 and 2 because they are considered negligible in these zones. Finally, blocks 3 and 4 are formed in the zoning program with a high degree of clustering in the direction normal to the wing surface to support the viscous terms in the boundary layer. Block 3 is on top of the wing and block 4 is below the wing.

Grids used for free-air calculations are the same as the wind-tunnel grids except additional grid points are added in block 1 upstream, downstream and outboard of the wing, see [Fig. (1c)].

Zonal Interface Conditions

All four zones overlap their adjacent zones by one or two cell widths, with the exception of the interface between blocks 3 and 4. The flow field is advanced to the next iteration level (or time level for time accurate computations) by first updating the flow field in all four zones. Boundary conditions are then applied to each zonal boundary by interpolating data from the interior of an adjacent zone. This process is repeated until a desired level of convergence is achieved. The solution variables at the interface between blocks 3 and 4 are obtained by averaging the flow variables about the interface plane, see [Fig. (1b)].

The boundary condition procedure between adjacent zones is illustrated in Fig. (2) by a hypothetical 2 zone topology. Zone 1 is a coarse grid while zone 2 has been refined by doubling the grid points in all three directions. A common interface surface between the two grids is shown in Fig. (2b). When data are transferred from zone 1 (coarse) to zone 2 (fine), linear interpolation is used. This is a nonconservative interpolation. When data are transferred from zone 2 (fine) to zone 1 (coarse), direct injection is used and is fully conservative.

Referring back to Fig. (1b), there is a one-to-one correspondence between blocks 2, 3, and 4 in the streamwise direction. Therefore, direct injection is used there, and shocks can pass through these zonal boundaries in a conservative manner.

BOUNDARY CONDITIONS

The TNS wing code presently has an option for treating inviscid wind-tunnel walls or free-air cases. For the wind-tunnel case, if one wishes to model viscous wind-tunnel walls (this has been done in the TNS aircraft code [6]), one could use additional zones near the walls with appropriate viscous clustering. However, in order to take advantage of the present 4 zone grid topology and avoid the additional resource penalties of more grid points, all wind-tunnel walls were treated as inviscid surfaces.

Flow symmetry was imposed at the wing root plane (splitter plate). This was accomplished by reflecting the grid one grid point about the wing root plane. The governing equations were solved at the symmetry plane, $k = 2$, and the flow solution reflected each

iteration from $k = 3$ into $k = 1$. This procedure is more accurate and stable than simply extrapolating the flow variables at the symmetry plane.

It was mentioned in the introduction that experimental data for all flow variables were available at the inflow boundary. However, because the wind-tunnel walls were treated as inviscid surfaces, it was decided to impose uniform flow conditions there. The experimental pressure was available at the outflow boundary. This information was used, together with the perfect gas law, and extrapolation, to obtain the solution variables at the outflow boundary.

The free-air boundary conditions were exactly the same as the wind-tunnel conditions with two exceptions: uniform flow was imposed at the far field, and the flow variables at the exit plane were obtained by extrapolation.

RESULTS AND DISCUSSION

Six workshop cases were investigated and reported in this paper. The flow conditions are summarized in Table 1. Each case has a freestream Mach number $M_\infty = 0.82$, and a Reynolds number based on wing root chord $Re = 3.6 \times 10^6$. The Reynolds number based on the mean geometric chord is $Re = 1.3 \times 10^6$ and is perhaps more indicative that the flow is transitional. The transition line (where the flow is considered fully turbulent) was provided from experimental data. This transition line was nominally at 60% chord along the wing span except near the root section where the flow was fully turbulent. The Baldwin-Lomax algebraic turbulence model was used to compute a turbulent eddy viscosity. Shang et al [17] describe an empirical transition model which they applied to supersonic flows. This model is based on the exponential function and requires a characteristic length. This information was not known apriori, so a cubic polynomial was used to allow smooth transition from laminar viscosity to turbulent viscosity over a specified number of grid points. The results for the six cases are described below.

Table 1 Wing flow fields investigated.

Case	M_∞	α°	Transition	Reynolds No.*	Grid Points
A1-Wind Tunnel	0.82	0	Modeled	3.6×10^6	337,000
A2-Wind Tunnel	0.82	2	Modeled	3.6×10^6	337,000
B1-Free Air	0.82	0	Modeled	3.6×10^6	415,000
B2-Free Air	0.82	2	Modeled	3.6×10^6	415,000
B3-Free Air	0.82	5	Fully Turbulent	3.6×10^6	415,000
B4-Free Air	0.82	8	Fully Turbulent	3.6×10^6	415,000

*Based on the wing root chord.

The first case, A1, is a simulation of a wing mounted in a wind tunnel with $\alpha = 0^\circ$. Computed oil-flow patterns and pressure contours for the upper wing surface are shown in Fig. (3). This first solution had a transition width of one grid point, i.e., the flow transitioned impulsively from laminar to turbulent flow. This was an extremely difficult case to converge, achieving a three-order reduction in the L_2 -norm of the residual for all

three blocks in approximately 3000 iterations. A separation line can be observed with reattachment near the wing root trailing edge. The normal grid spacing is relatively fine (average $y^+ = 1.2$ for all cases), and the vertical extent of separation near the wing root was small (3 to 4 grid points). However, there was a large vertical extent of separation where the separation line moves upstream. This result was rather surprising for $\alpha = 0^\circ$ angle of attack. A shock wave can be observed in Fig. (3b). Notice that the shock moves forward with the separation line. This indicates a strong shock boundary-layer interaction. When the flow field was recomputed with a transition width of 5 grid points, convergence was achieved rapidly (1100 iterations). This solution is shown in Fig. (4) which includes the C_p variation at various spanwise locations, simulated oil-flow patterns and surface pressure contours on the upper wing surface. In this case, the shock extends along the wing span and moves slightly upstream near the wing tip. The separation pattern also extends along the wing span except near the wing tip. The vertical extent of this separation is small (3 to 4 grid points). Again, as with all cases described in this paper, the average y-plus was $y^+ = 1.2$. Recomputing this case again with a 10 grid point transition width did not show any further changes in the solution. Moreover, when the flow was treated as a fully turbulent case, the results were similar (except near the wing tip) to the 5 grid point transitional flow. Therefore, the 5 grid point transitional model seemed adequate and was used for all further computations.

Case B1 is a free-air computation at $\alpha = 0^\circ$. The oil-flow patterns in Fig. (5) indicate that the flow is attached and the shock position is similar to the wind-tunnel case, although the shock did not move upstream near the wing tip as it did in the wind-tunnel case. This shows some of the effects of the wind-tunnel walls.

From the above flow simulations, it is apparent that knowing the location of turbulent transition was not sufficient and the history of turbulent transition must be properly modeled. Allowing turbulent transition over several grid points was at best ad hoc, but because the wind-tunnel flow underwent free turbulent transition, the present model of transitioning over a length of 5 grid points is probably more realistic than an impulsive transition. Clearly, this issue requires further investigation.

Case A2 is a wind-tunnel simulation at $\alpha = 2^\circ$. The results are shown in Fig. (6). Once again, the separation line extends along the wing span approximately parallel with the trailing edge. This is a predominantly shock-induced separation as seen by the shock position in Fig. (6c). Near the wing tip the separation line moves much closer to the trailing edge. Notice the relatively constant pressure region behind the shock at 65% semi-span. The maximum residual occurs here, and this case never converged. The flow appears to be unsteady, mostly because of the large extent of separation interacting with the shock, see [Fig. (7)]. An effort was made to simulate this flow in a time-accurate fashion, however, the fine grid clustering required a small time step ($\Delta t = 0.002$) for stability reasons. This was much too costly to pursue and was therefore abandoned.

Case B2 is a free-air simulation at $\alpha = 2^\circ$. This case converged to a steady state without any difficulty. It can be seen from the oil-flow patterns in Fig. (8) that the region of separation is greatly reduced from the wind-tunnel case. The separation is mostly near the wing root area and the vertical extent of separation is small (4 to 5 grid points). The flow at 65% semi-span appears to be on the verge of separating, or it has separated and immediately reattached depending on how one interprets the oil-flow patterns.

The difference between the wind-tunnel case, A2, and the free-air case, B2, is attributed mostly to the outflow boundary conditions. In order to verify this assertion, case A2 was recomputed with different outflow boundary conditions. The same wind-tunnel grid was used with the exception that grid points were added downstream of the exit plane so that the outflow boundary was 4 root chords downstream of the wing root section. Upstream of the wind-tunnel exit plane, the grid is identical to case A2. The same turbulence and turbulent transition models were used as in case A2. Moreover, the inflow, wind-tunnel walls, and splitter-plate boundary conditions were identical to case A2. The only difference is that extrapolation boundary conditions were employed at the outflow boundary. Thus, this case is identical to case A2 with the exception of the flow conditions at the wind-tunnel exit plane. This resulted in a steady solution (as in the free-air case) and converged easily in 1400 iterations.

Figure (9) shows a significant difference in C_p contours at the wind-tunnel exit plane. Notice that the experimental pressure specified at the wind-tunnel exit plane does not vary in the vertical direction but only in the spanwise direction, [see Fig. (9a)]. One would expect to see some wake effects and the presence of a wing-tip vortex because the wind-tunnel exit plane is only 0.75 root chords downstream of the wing root trailing edge. On the other hand, the effects of the wing-tip vortex can be seen in the recomputed case, Fig. (9b), along the $C_p = -0.005$ contour line. Notice in this case the C_p contours do show pressure variation in the vertical direction and a compression region directly behind the wing root section, as expected. The exit-plane C_p contours for the free-air case, B2, are similar to those in Fig. (9b).

The pressure data at the outflow boundary provided by experiment is exactly the same for both the $\alpha = 0^\circ$ and $\alpha = 2^\circ$ cases. It is therefore clear that this experimental pressure specified at the wind-tunnel exit plane is inadequate for an accurate wind tunnel flow simulation. Either more precise pressure data is required, or the experimental pressure field should be given farther downstream of the wing trailing edge. Figure (10) shows the convergence history for the wind-tunnel and free-air cases. Note the oscillatory behavior in the wind-tunnel case and the rapid convergence for the free-air case.

Case B3 is a free-air simulation at $\alpha = 5^\circ$. This computation was treated as fully turbulent, and the results are shown in Fig. (11). The computed oil-flow pattern indicates a large region of shock induced separation. The separation line is significantly upstream of the $\alpha = 2^\circ$ case. A line of separation, reattachment, and another separation line can be seen near the wing tip.

Case B4 is the last free-air simulation at $\alpha = 8^\circ$. This also was treated as a fully turbulent flow. The shock near the root section is relatively weak but becomes much stronger outboard of the root section, see Fig. (12). A large region of shock induced separation is evident in the computed oil-flow patterns. There are two saddle point singularities along the main separation line.

Figure (10) summarizes the variation of lift coefficient with angle of attack and with drag coefficient. The nonlinearity of the C_L vs α curve is evident and is largely due to the complex separation seen at higher angles of attack. The lift coefficient for the free-air and wind-tunnel cases at $\alpha = 2^\circ$ are nearly equal, however, the drag coefficient for the wind-tunnel cases is significantly greater than the free-air cases. This is to be expected because the presence of wind-tunnel walls result in stronger shocks and, hence, greater wave drag.

Finally, Table 2 summarizes the convergence history and computer time for all the cases presented in this paper.

Table 2 Summary of convergence and CPU time.

Case	α°	Iterations*	CPU-hr**
A1	0	1100	3.4
A2	2	Unsteady?	—
B1	0	1200	4.5
B2	2	1300	4.9
B3	5	1400	5.3
B4	8	1400	5.3

*To achieve a 3 order reduction in the L_2 -norm of the residual in all 4 zones.

**Cray 2 time.

CONCLUDING REMARKS

Navier-Stokes simulations of flow fields about the DFVLR-F5 wing at wind-tunnel and free-air conditions have been computed using the TNS code on NAS' Cray 2 at NASA Ames Research Center. These computations have been performed to help assess the current state-of-the-art capabilities of predicting wing flow fields with viscous CFD codes. Three dimensional grid generation is still in the developmental stage and proved to be tedious when applied to the DFVLR-F5 wing geometry. The flow field was sensitive to the treatment of turbulent transition. Even with an apriori knowledge of the transition line, the modeling of the transition width can significantly affect the flow simulation. Clearly, additional work is required to adequately model turbulence and turbulent transition for practical wing flows.

Unsteady flow was observed for the $\alpha = 2^\circ$ wind-tunnel case but not for the corresponding free-air case. The specification of the experimental pressure at the wind-tunnel exit plane was shown to be the primary reason for this difference. Future experiments designed for code calibration should supply exit plane data farther downstream from the wing trailing edge.

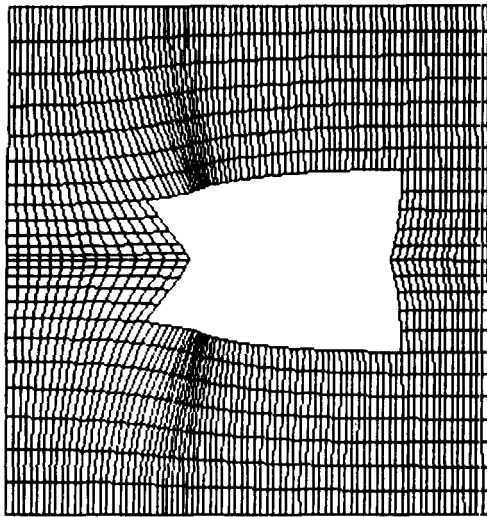
ACKNOWLEDGEMENT

The author would like to thank Mr. Reese Sorenson of NASA Ames Research Center for his assistance in grid generation.

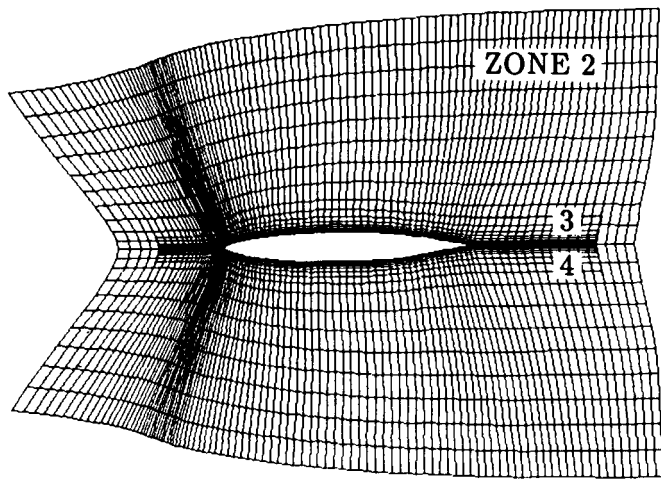
REFERENCES

- [1] KUTLER, P.: "A perspective of theoretical and applied computational fluid dynam-

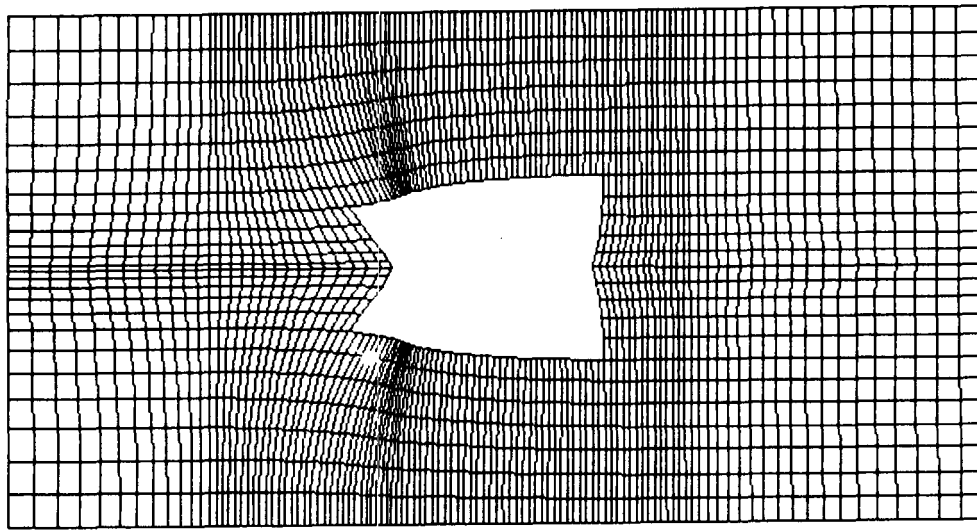
- ics," AIAA Paper 83-0037, 1983.
- [2] CHAPMAN, D. R.: "Trends and pacing items in computational aerodynamics," **Lecture Notes in Physics**, Vol. 141, edited by W. C. REYNOLDS and R. W. MACCORMACK, 1981.
 - [3] SRINIVASAN, G. R., MCCROSKEY, W. J., BAEDER, J. D., EDWARDS, T. A.: "Numerical simulation of tip vortices of wings in subsonic and transonic flows," AIAA Paper 86-1095, 1986.
 - [4] FUJII, K., SCHIFF, L. B.: "Numerical simulation of vortical flows over a strake-delta wing," AIAA Paper 87-1229, 1987.
 - [5] KAYNAK, U., FLORES, J.: "Advances in the computation of transonic separated flows over finite wings," AIAA Paper 87-1195, 1987.
 - [6] FLORES, J., CHADERJIAN, N. M., SORENSON, R. L.: "Simulation of transonic viscous flow over a fighter-like configuration including inlet," AIAA Paper 87-1199, 1987.
 - [7] HOLST, T. L., KAYNAK, U., GUNDY, K., THOMAS, S. D., FLORES, J., CHADERJIAN, N. M.: "Transonic wing flows using an Euler/Navier-Stokes zonal approach," **Journal of Aircraft**, Vol. 24, No. 1, January 1987, pp. 17-24.
 - [8] BALDWIN, B. S., LOMAX, H.: "Thin-layer approximation and algebraic model for separated turbulent flows," AIAA Paper 78-257, Jan. 1978.
 - [9] SOBIECZKY, H.: "DFVLR-F5 test wing configuration for computational and experimental aerodynamics," preprint for workshop participants, IB 221 - 87 A 01, Feb., 1987.
 - [10] SORENSON, R. L.: "Three-dimensional elliptic grid generation about fighter aircraft for zonal finite-difference computations," AIAA Paper 86-0429, 1986.
 - [11] BEAM, R., WARMING, R. F.: "An implicit factored scheme for the compressible Navier-Stokes equations," AIAA Paper 77-645, June 1977.
 - [12] CHADERJIAN, N. M.: "Transonic Navier-Stokes wing solutions using a zonal approach, Part 2. High angle-of-attack simulation," AGARD CP 412, Applications of Computational Fluid Dynamics in Aeronautics, Paper 30B, April 1986; also NASA TM 88248, April 1986.
 - [13] PULLIAM, T. H., STEGER, J. L.: "Implicit finite-difference simulations of three-dimensional compressible flow," **AIAA Journal**, Vol. 18, No. 2, Feb. 1980, pp. 159-167.
 - [14] PULLIAM, T. H., CHAUSSEE, D. S.: "A diagonal form of an implicit approximate-factorization algorithm," **Journal of Computational Physics**, Vol. 39, No. 2, 1981, pp. 347-363.
 - [15] SRINIVASAN, G. R., CHYU, W. J., STEGER, J. L.: "Computation of simple three-dimensional wing-vortex interaction in transonic flow," AIAA Paper 81-1206, June 1981.
 - [16] FLORES, J.: "Convergence acceleration for a three-dimensional Euler/Navier-Stokes zonal approach," **AIAA Journal**, Vol. 24, No. 9, Sept. 1986, pp. 1441-1442.
 - [17] SHANG, J. S., HANKYEY, W. L., PETTY, J. S.: "Three-dimensional supersonic interacting turbulent flow along a corner," AIAA Paper 78-1210, July 1978.



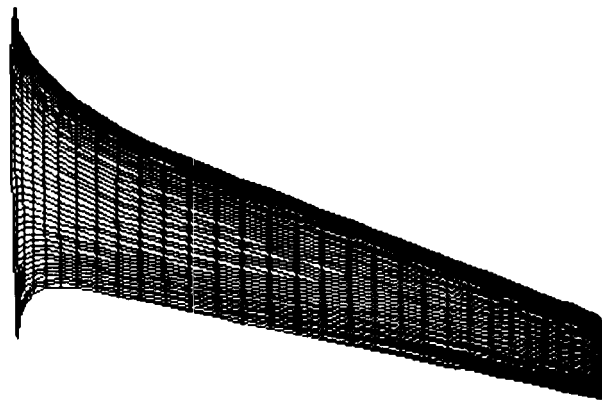
a) Zone 1 - Wind-tunnel case.



b) Zones 2, 3, and 4.

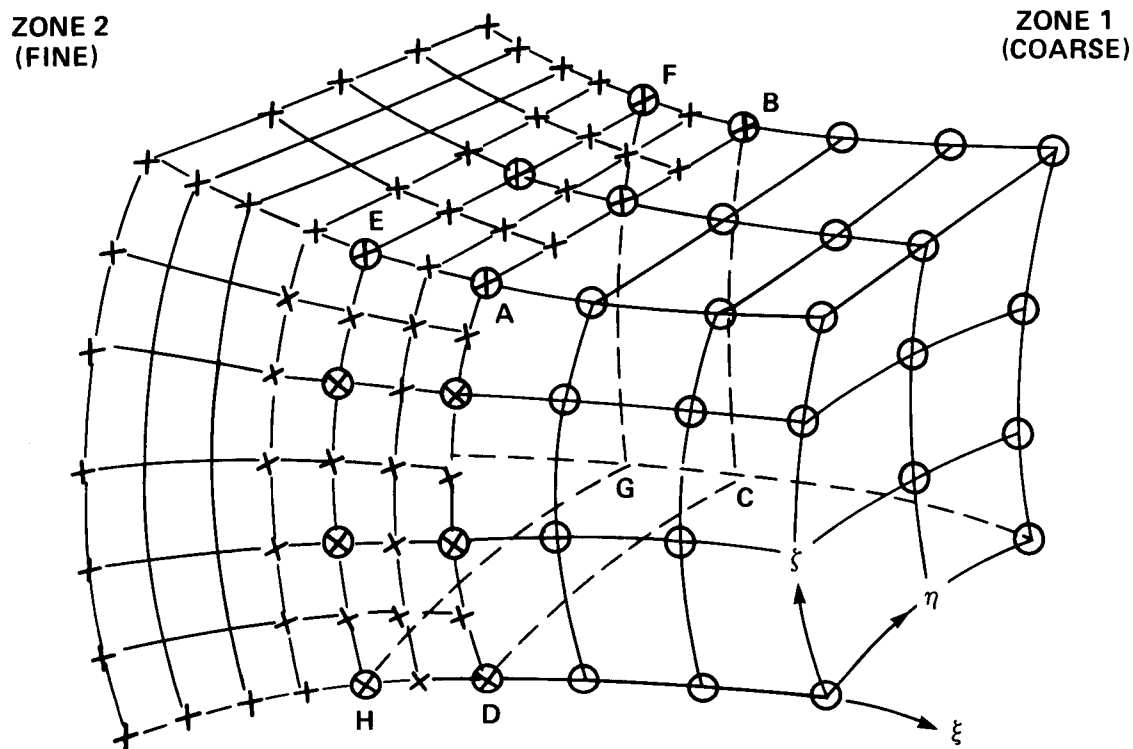


c) Zone 1 - Free-air case.

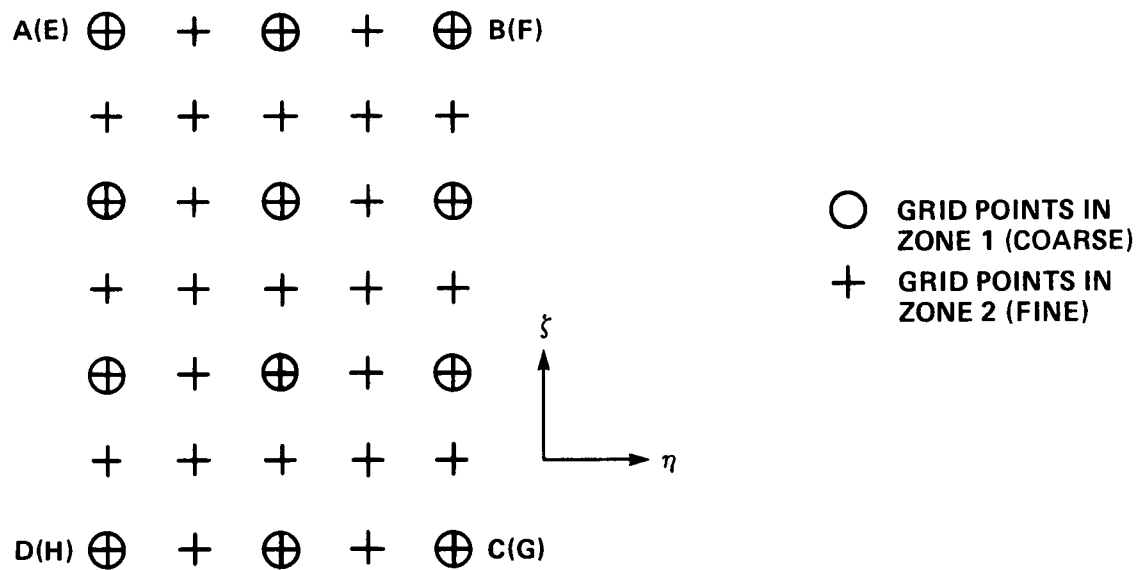


d) Grid on upper wing surface (55x35).

Fig. (1) Zonal grid topology.

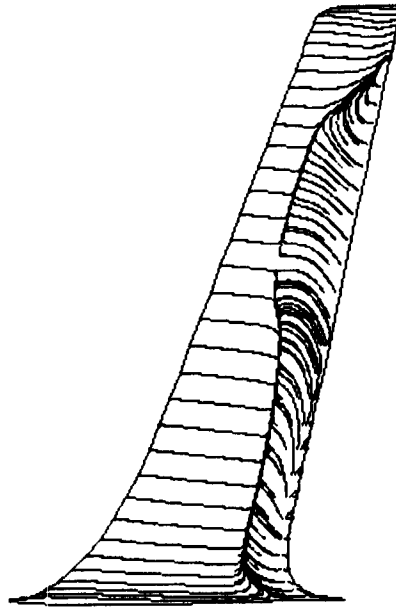


(a) TWO-ZONE GRID SHOWING OVERLAP AT ABCD AND EFGH PLANES IN PHYSICAL SPACE

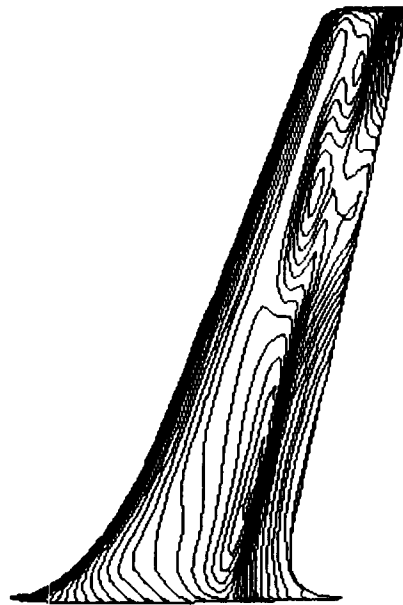


(b) GRID POINT DETAIL IN THE OVERLAP REGION IN TRANSFORMED SPACE.

Fig. (2) Zonal interfacing between to hypothetical zones.

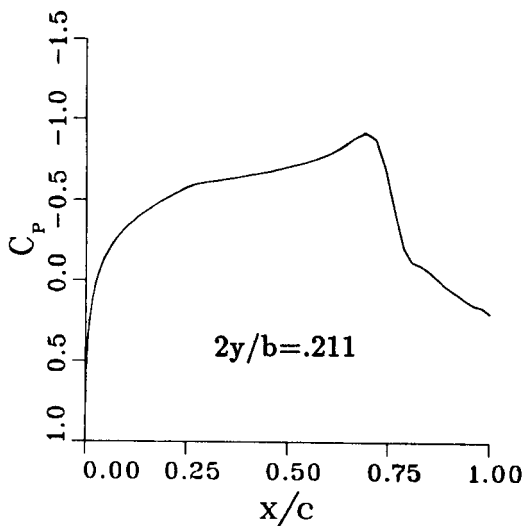
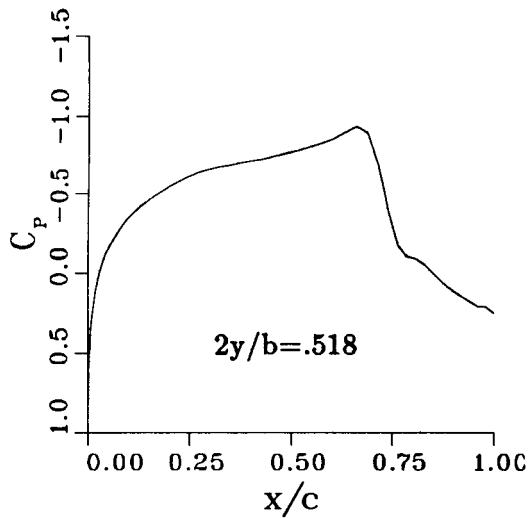
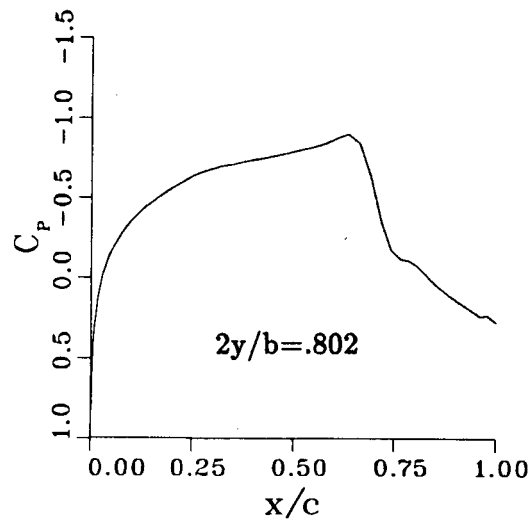


a) Simulated oil flow on upper wing surface.

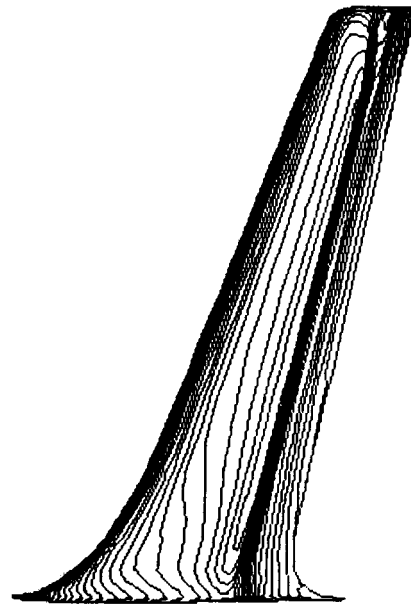


b) Pressure contours on upper wing surface.

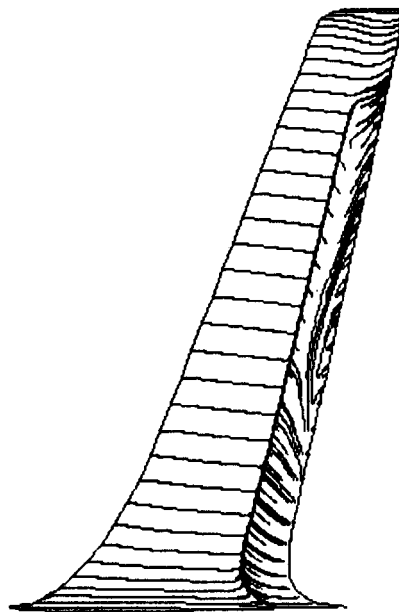
Fig. (3) Wind-tunnel case (A1) with $M_\infty = .82$, $\alpha = 0^\circ$, $Re = 3.6 \times 10^6$, transition width = 1 grid point.



a) Pressure coefficient.

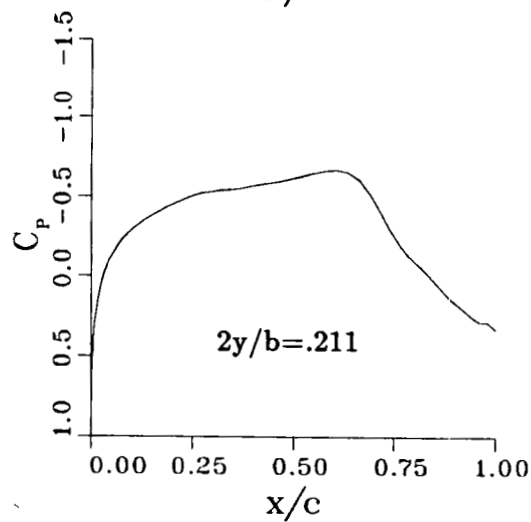
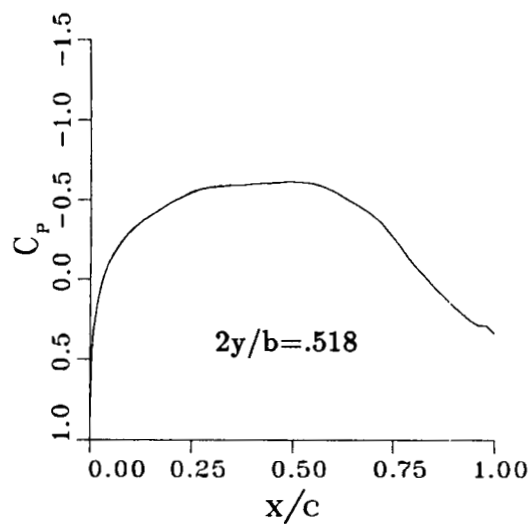
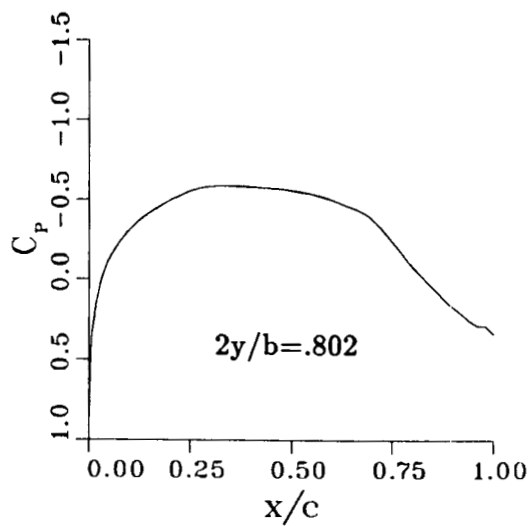


b) Pressure contours on upper wing surface.

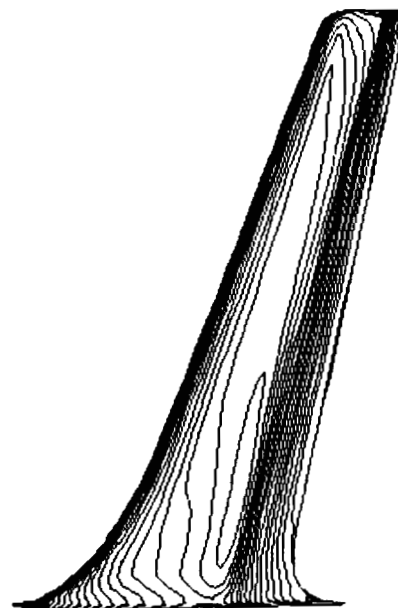


c) Simulated oil flow on upper wing surface.

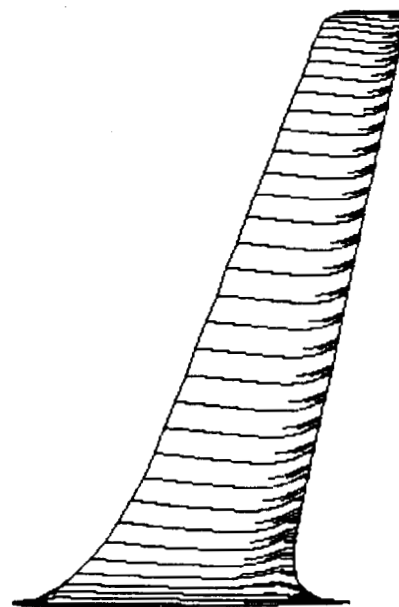
Fig. 4) Wind-tunnel case (A1) with $M_\infty = .82$, $\alpha = 0^\circ$, $Re = 3.6 \times 10^6$, transition modeled.



a) Pressure coefficient.

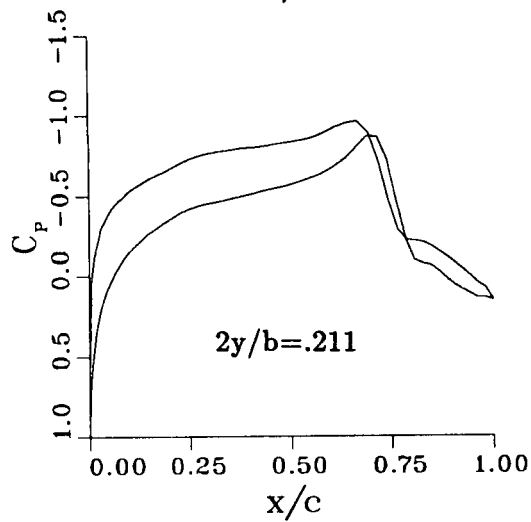
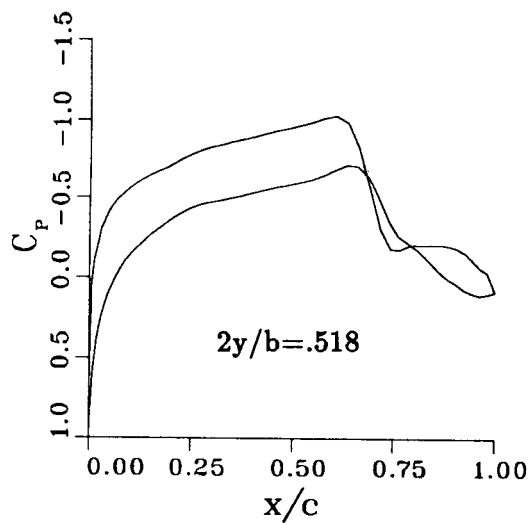
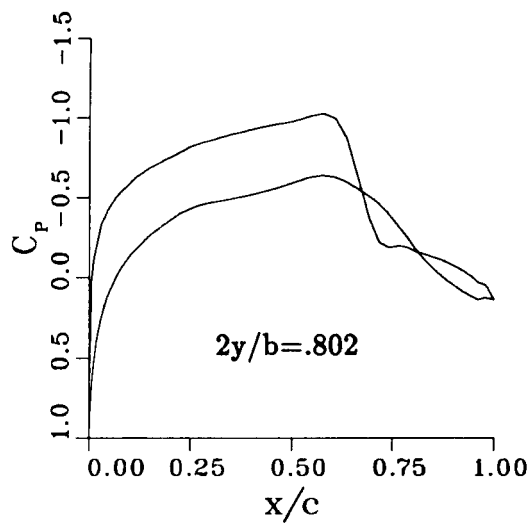


b) Pressure contours on upper wing surface.

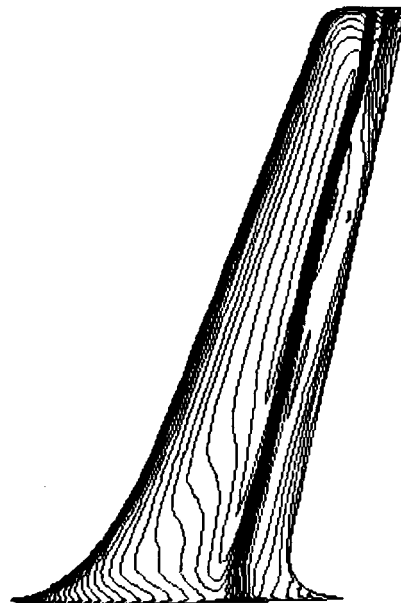


c) Simulated oil flow on upper wing surface.

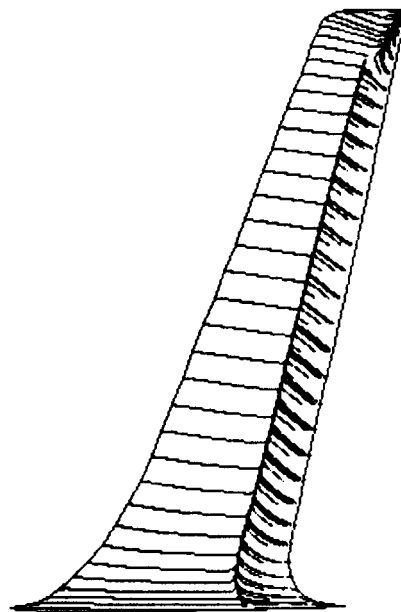
Fig. 5) Free-air case (B1) with $M_\infty = .82$, $\alpha = 0^\circ$, $Re = 3.6 \times 10^6$, transition modeled.



a) Pressure coefficient.



b) Pressure contours on upper wing surface.



c) Simulated oil flow on upper wing surface.

Fig. 6) Wind-tunnel case (A2) with $M_\infty = .82$, $\alpha = 2^\circ$, $Re = 3.6 \times 10^6$, transition modeled.

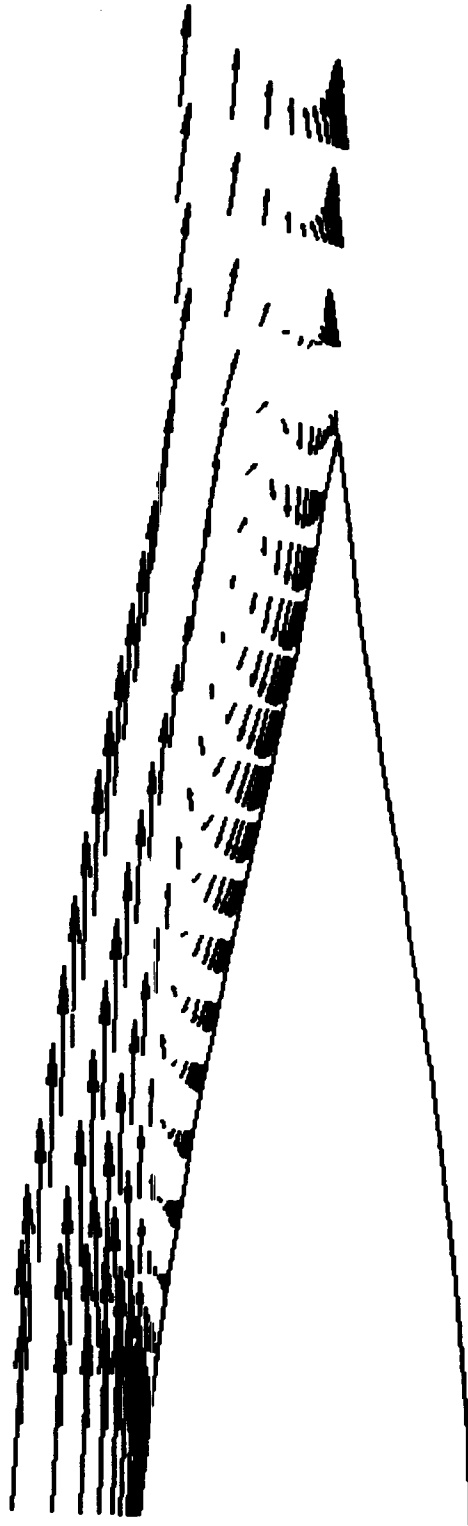
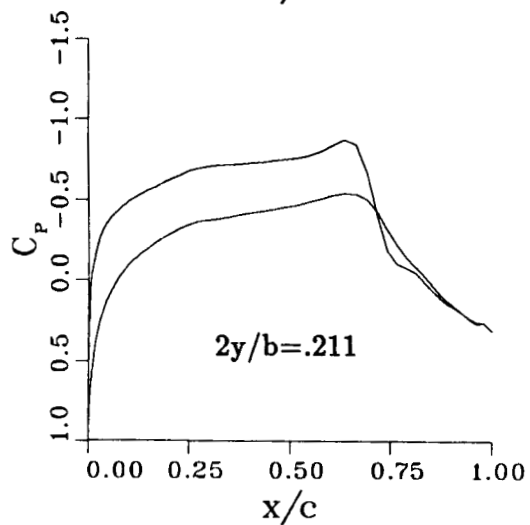
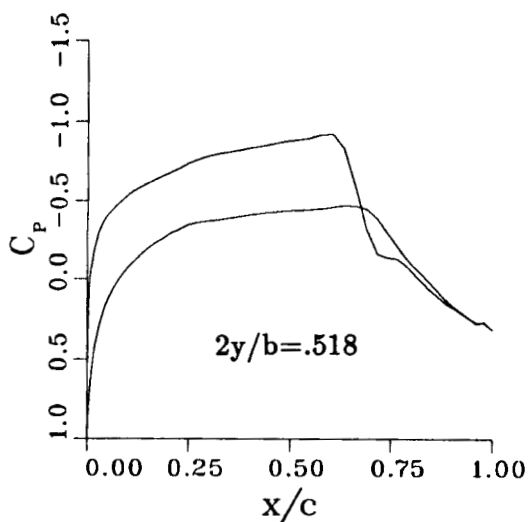
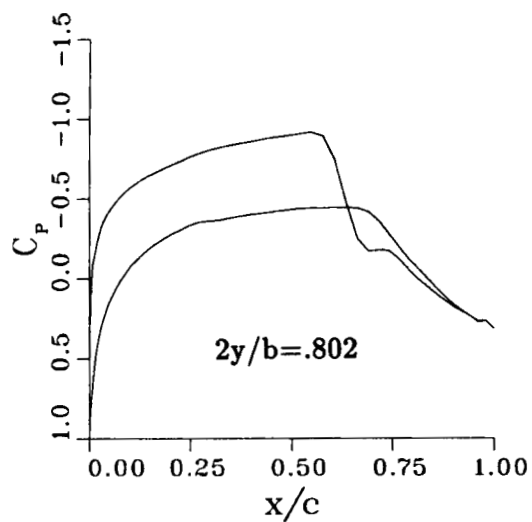
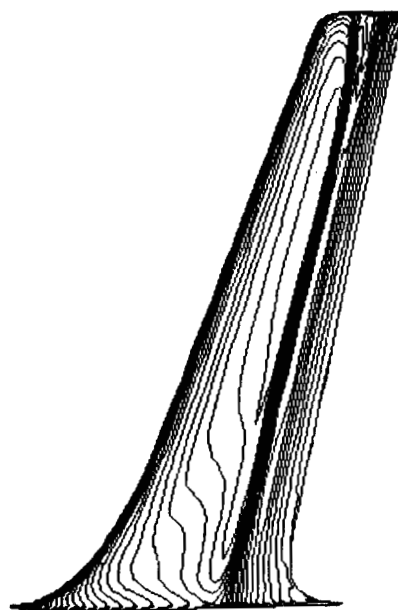


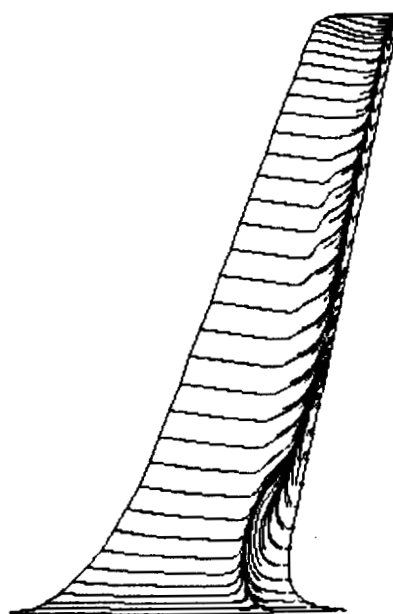
Fig. (7) Case A2: velocity vectors at 65% semi-span.



a) Pressure coefficient.

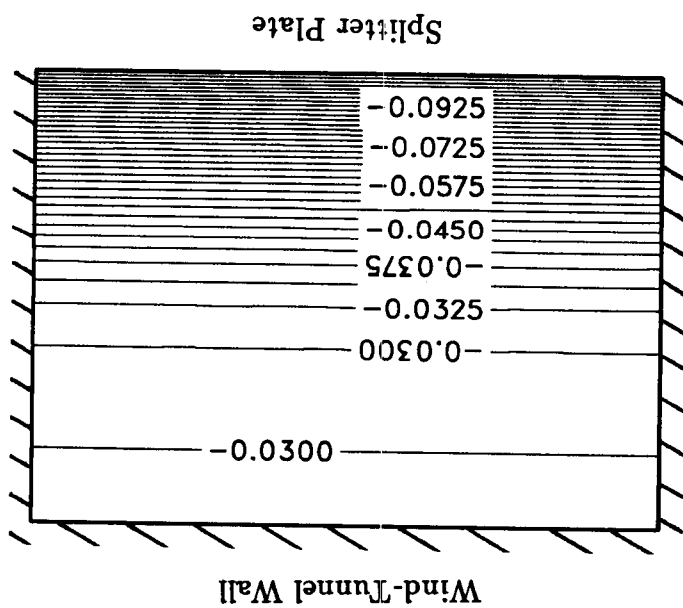


b) Pressure contours on upper wing surface.

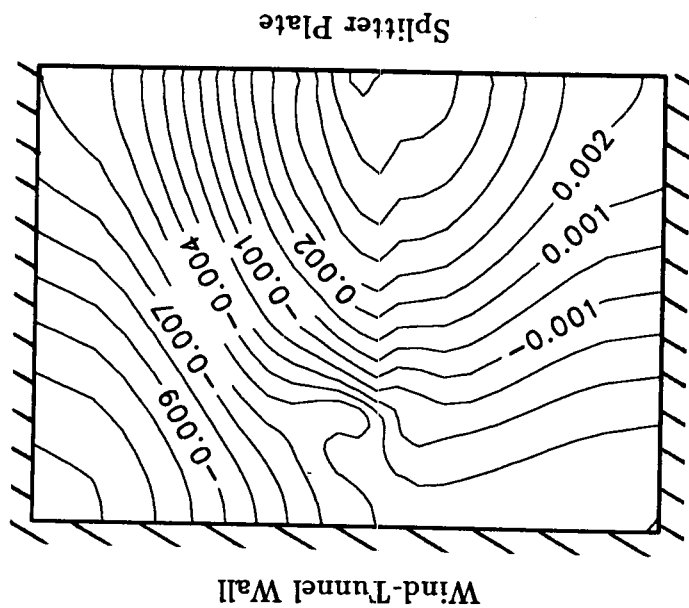


c) Simulated oil flow on upper wing surface.

Fig. 8) Free-air case (B2) with $M_\infty = .82$, $\alpha = 2^\circ$, $Re = 3.6 \times 10^6$, transition modeled.

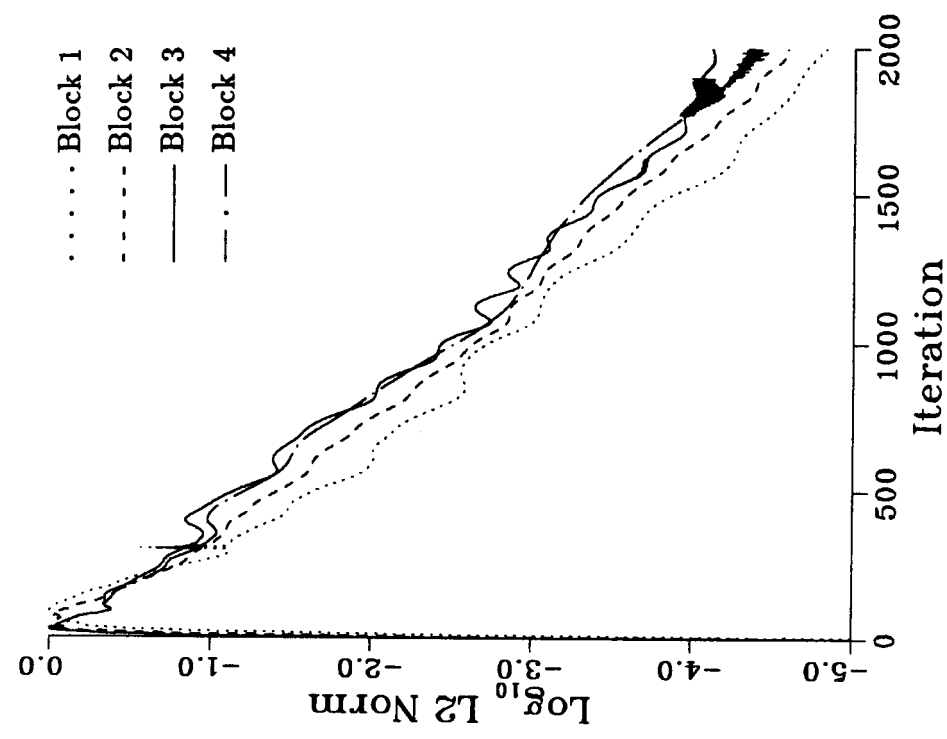


a) Wind-tunnel grid with experimental C_p specified at wind-tunnel exit plane.

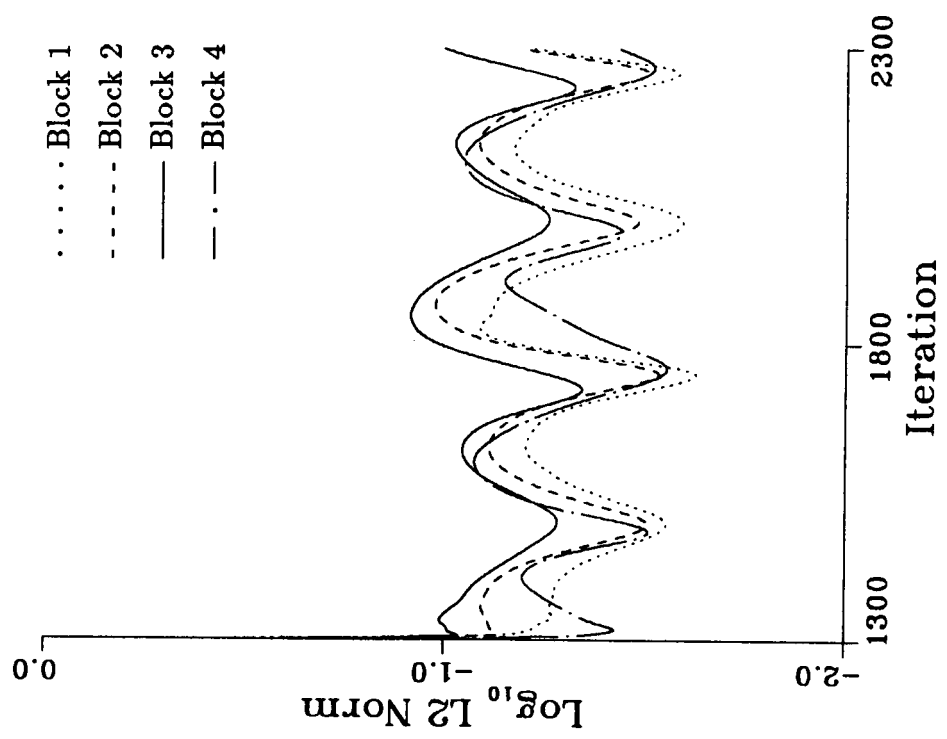


b) Wind-tunnel grid with grid extension downwind of wind-tunnel exit plane. Flow variables determined at outflow boundary by extrapolation.

Fig. (9) Cross-sectional view of C_p contours at wind-tunnel exit plane.

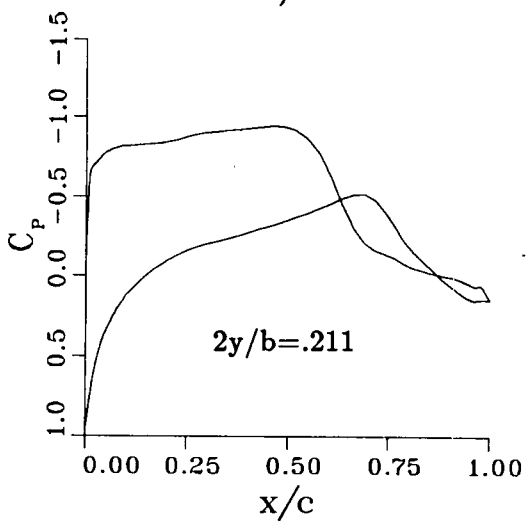
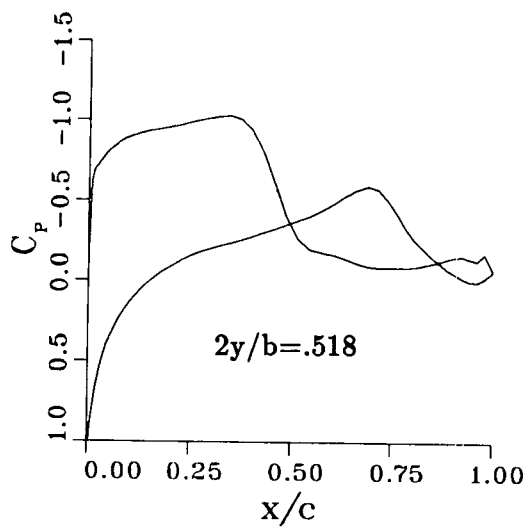
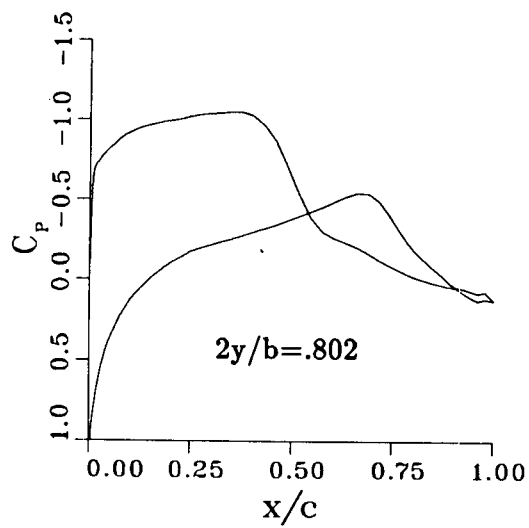


b) Free-air case, $\alpha = 2$.

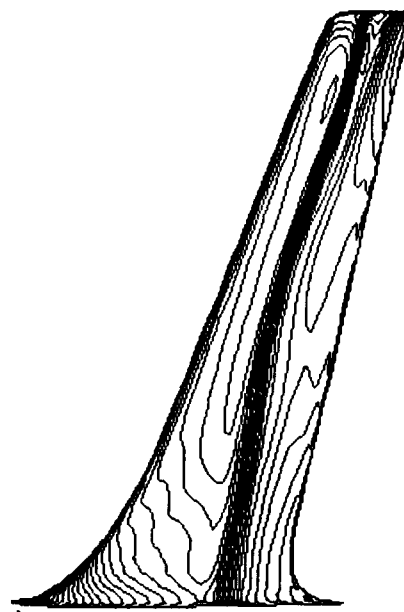


a) Wind-tunnel case, $\alpha = 2$.

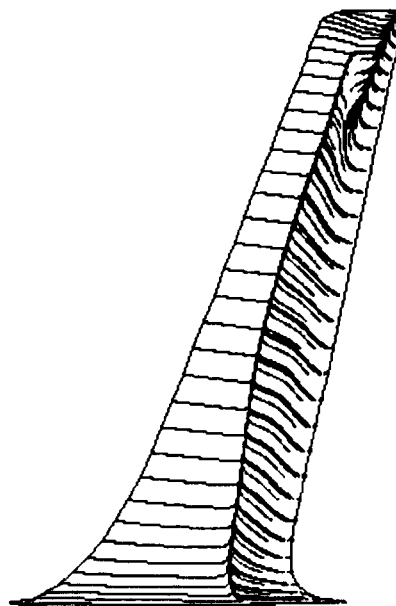
Fig. (10) Residual convergence history.



a) Pressure coefficient.

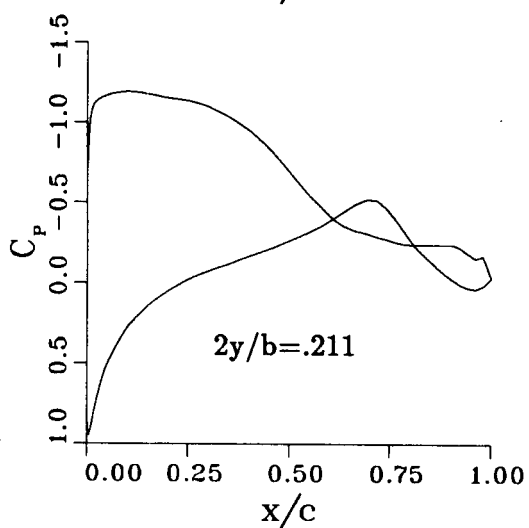
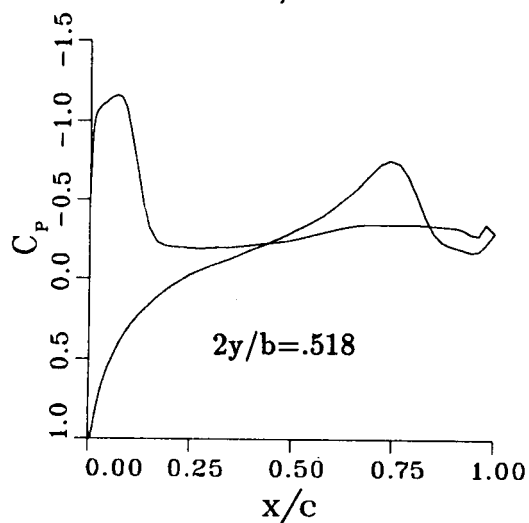
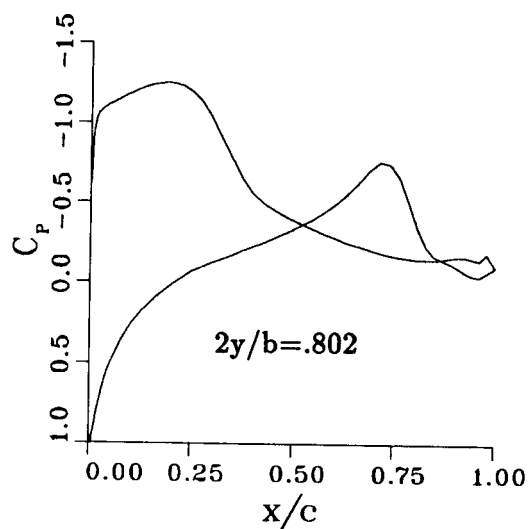


b) Pressure contours on upper wing surface.

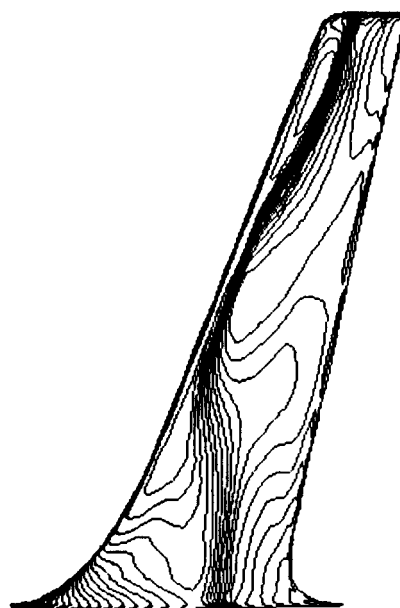


c) Simulated oil flow on upper wing surface.

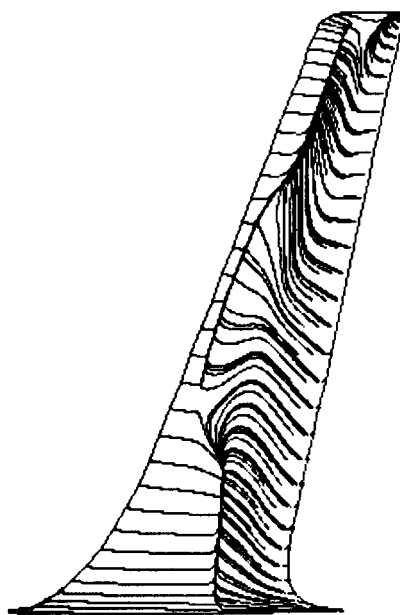
Fig. 11) Free-air case (B3) with $M_\infty = .82$, $\alpha = 5^\circ$, $Re = 3.6 \times 10^6$, fully turbulent.



a) Pressure coefficient.

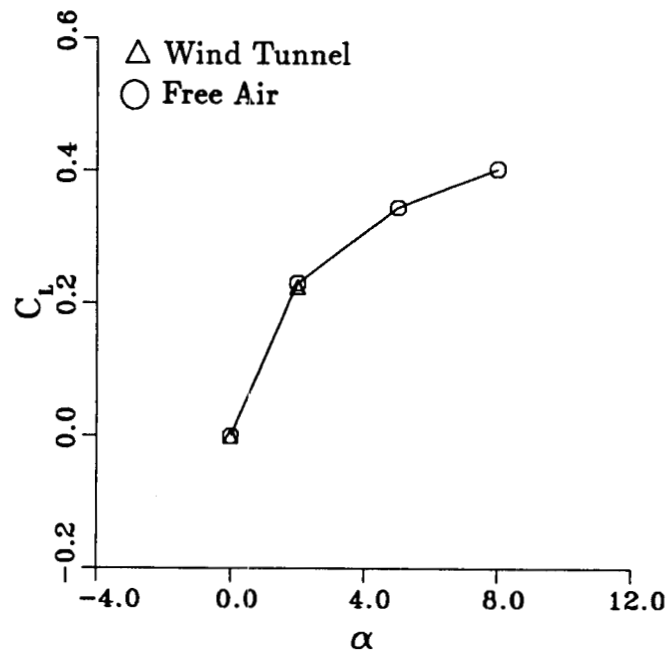


b) Pressure contours on upper wing surface.

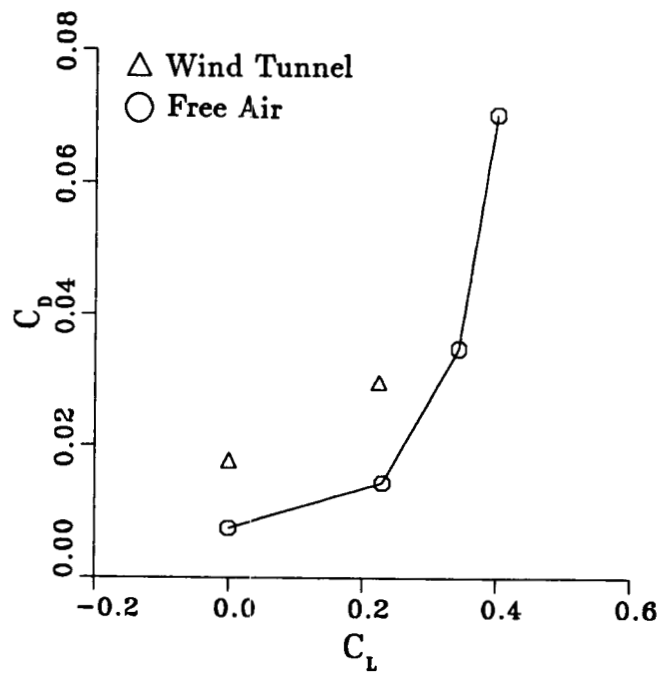


c) Simulated oil flow on upper wing surface.

Fig. 12) Free-air case (B4) with $M_\infty = .82$, $\alpha = 8^\circ$, $Re = 3.6 \times 10^6$, fully turbulent.



a) C_L vs α curve.



b) C_D vs C_L curve.

Fig. (13) Lift and drag coefficients for wind-tunnel and free-air cases.



Report Documentation Page

1. Report No. NASA TM-100039	2. Government Accession No.	3. Recipient's Catalog No.	
4. Title and Subtitle Navier-Stokes Simulation of Transonic Wing Flow Fields Using a Zonal Grid Approach		5. Report Date January 1988	
		6. Performing Organization Code	
7. Author(s) Neal M. Chaderjian		8. Performing Organization Report No. A-88020	
		10. Work Unit No. 505-60	
9. Performing Organization Name and Address Ames Research Center Moffett Field, CA 94035		11. Contract or Grant No.	
		13. Type of Report and Period Covered Technical Memorandum	
12. Sponsoring Agency Name and Address National Aeronautics and Space Administration Washington, DC 20546-0001		14. Sponsoring Agency Code	
15. Supplementary Notes Point of Contact: Neal M. Chaderjian, Ames Research Center, MS 258-1, Moffett Field, CA 94035 (415) 694-6416 or FTS 464-6416			
16. Abstract <p>The transonic Navier-Stokes code was used to simulate flow fields about isolated wings for workshop wind-tunnel and free-air cases using the thin-layer Reynolds-averaged Navier-Stokes equations. An implicit finite-difference scheme based on a diagonal version of the Beam-Warming algorithm was used to integrate the governing equations. A zonal grid approach was used to allow efficient grid refinement near the wing surface. The flow field was sensitive to the turbulent transition model, and flow unsteadiness was observed for a wind-tunnel case but not for the corresponding free-air case. The specification of experimental pressure at the wind-tunnel exit plane is the primary reason for the difference of these two numerical solutions.</p>			
17. Key Words (Suggested by Author(s)) Navier-Stokes Wing Computational fluid dynamics Separation Transonic flow Turbulent transition		18. Distribution Statement Unclassified – Unlimited Subject Category – 02	
19. Security Classif. (of this report) Unclassified	20. Security Classif. (of this page) Unclassified	21. No. of pages 24	22. Price A02